powders

Review

Are Drag Models Adequate? A Comprehensive Analysis of Drag Modelling for Regular and Irregular Particles

Sadaf Maramizonouz and Sadegh Nadimi *

School of Engineering, Newcastle University, Newcastle upon Tyne NE1 7RU, UK; sadaf.maramizonouz@newcastle.ac.uk
* Correspondence: sadegh.nadimi-shahraki@ncl.ac.uk

Abstract

Particles travelling within and interacting with any fluid media are found in both natural phenomena and industrial processes. Through these interactions, the particles experience a drag force, heavily influenced by their morphology, and significantly affecting their dynamics. This study examines the relationship between particle morphology and the drag force exerted on them, using both empirical models and computational simulations. The findings indicate that for regular and irregular particles of diverse morphologies, a combination of existing empirical models can predict the drag force within a 40% error margin. However, these models may fall short of meeting the accuracy demands in certain applications. To address this, the study provides clear guidelines for selecting the most suitable drag model based on particle morphology and flow regime.

Keywords: drag force; drag coefficient; particle morphology; irregular particle

1. Introduction

Particulate materials are an inseparable part of nature and thus are encountered extensively in various scientific fields and industries. This not only includes everyday applications like food [1], medicine [2], transport [3], and cosmetics [4] but also advanced technologies, such as space exploration [5]. When particles transport through liquids or gases, forces and moments in different directions are exerted on them. The drag force, $\boldsymbol{F}_D$, is often proposed as the most important force the particles experience since it governs the majority of the particle dynamics and is defined as [6,7]:

$$\boldsymbol{F}_D = \frac{1}{2}\rho_f A \left|\boldsymbol{U}_p - \boldsymbol{U}_f\right| \left(\boldsymbol{U}_p - \boldsymbol{U}_f\right) C_D \tag{1}$$

where ρ_f is the fluid density, A is the particle reference area, and $\boldsymbol{U}_p$ and $\boldsymbol{U}_f$ are the velocity of the particle and the fluid, respectively. C_D is the particle drag coefficient which for spherical particles is only a function of the particle Reynolds number, Re. The Reynolds number defines the flow regime that the particle experiences and is determined as:

$$Re = \frac{\rho_f \left|\boldsymbol{U}_p - \boldsymbol{U}_f\right| d}{\mu_f} \tag{2}$$

where d is the particle reference length (diameter for spherical particles) and μ_f is the fluid viscosity. For particles with more complicated morphologies, estimating the drag coefficient while accounting for their morphology is the most challenging in modelling the

check for updates

Academic Editor: Sergiy Antonyuk

Received: 30 July 2025
Revised: 9 October 2025
Accepted: 17 October 2025
Published: 5 November 2025

Citation: Maramizonouz, S.; Nadimi, S. Are Drag Models Adequate? A Comprehensive Analysis of Drag Modelling for Regular and Irregular Particles. *Powders* **2025**, *4*, 29. https://doi.org/10.3390/powders4040029

drag force [8]. Considerable research has been performed to develop models for evaluating the drag coefficient of non-spherical particles and thus determining their dynamics and behaviour [8–21].

Our recent literature review focused on modelling the behaviour of particulate materials by coupling Computational Fluid Dynamics (CFD) to Discrete Element Method (DEM) showed that in ~90% of the studies, the particles' morphologies are simplified to spheres. A detailed breakdown of the frequency percentage of the spherical drag coefficient models [22–33] used in the above scientific articles are presented in Figure 1a, showing that the model by Gidaspow [22] is the most popular, followed by the model by Di Felice [23]. In this literature review, around 800 scientific articles published in 14 academic journals, namely *Powder Technology*, *Advanced Powder Technology*, *Particuology*, *Granular Matter*, *Computers and Geotechnics*, *Géotechnique*, *Chemical Engineering Journal*, *Journal of Computational Physics*, *Computational Particle Mechanics*, *Computer Methods in Applied Mechanics and Engineering*, *International Journal of Heat and Mass Transfer*, *Journal of Aerosol Science*, *Aerosol Science and Technology*, and *International Journal of Multiphase Flow*, were reviewed. It was found that only around 90 of the 800 reviewed scientific articles (~10%) utilise drag models that consider the effect of particles' morphology. Figure 1b shows the frequency percentage of the non-spherical drag coefficient models used in the CFD-DEM investigations. The models by Hölzer and Sommerfeld [12], Haider and Levenspiel [9], and Ganser [10] are the most favoured among the nine models used. All three of these most used models utilise the particles' true sphericity [34] to account for their morphology.

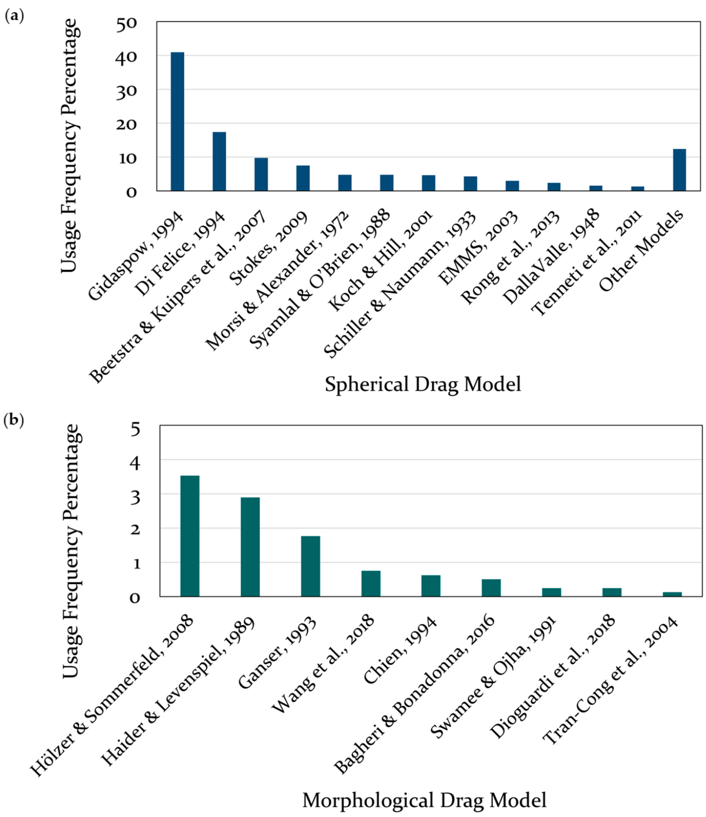

Figure 1. Frequency percentage of the usage of the (**a**) spherical [22–33] and (**b**) morphological [8–10,12–14,17,19,20] drag coefficient models in CFD-DEM modelling of the fluid-particle interactions.

The aim of the current work is twofold: first, to introduce a clear guide on how to choose the most accurate empirical drag model for non-spherical particles based on their morphological characteristics over a wide range of the Reynolds number for which

CFD results are provided as illustrative benchmarks; and second, to present when it is appropriate to simplify the particle morphology to a single sphere, which can be used in particular for CFD-DEM modelling of particles.

There is a spectrum of methods for modelling the particle drag force through computational modelling. The most accurate fully resolved method is Direct Numerical Simulation (DNS), which resolves all scales of particle-fluid interactions without empirical assumptions but is extremely costly in terms of computational resources and thus not accessible to a broad spectrum of users. The slightly less accurate but more practical methods are the Lattice Boltzmann Methods (LBM) and the Immersed Boundary Methods (IBM). CFD modelling, which solves the Navier-Stokes equations and is widely used due to the balance it offers between accuracy and computational cost. The empirical correlation methods, which are the least accurate but most computationally efficient, are typically used in large-scale multiphase simulations such as the many DEM models reviewed in the current work, where detailed resolution offered by DNS through CFD, although desirable, is often impractical due to large number of the particles being investigated.

2. Methodology

2.1. Classification of Particle Morphology

The morphology of particles plays a significant role in their mechanical, hydrological, rheological, and chemical behaviour and, therefore, should be considered in numerical simulations. In this work, eight particles of several origins, namely, natural sand, recycled crushed glass (RCG) granules [35], and rice grain are selected.

The three-dimensional morphology of these particles is obtained by performing X-ray micro-Computed Tomography (μCT) scans. The particles are scanned using the μCT system (SkyScan 1176, Bruker, Massachusetts, USA), located in the Preclinical in-Vivo Imaging Facility at Newcastle University Medical School, UK. The particles are then classified into four morphological categories of compact, flat, elongated, and bladed based on the Zingg [36] framework, which was then refined by Angelidakis et al. [37]. This framework categorised the particles based on their three orthogonal dimensions, namely, the short S, the intermediate I, and the long L dimension as well as the two aspect ratios of $\bar{e} = {}^{I}/_{L}$ and $\bar{f} = {}^{S}/_{I}$. Finally, all particles are scaled to have equal volumes of $\forall = 4.13 \times 10^{-8}$ m^2 and thus their diameter of the volume equivalent sphere (length scale) $d = 4.29 \times 10^{-3}$ m is equal. The five particles presented in Figure 2 are chosen to investigate the effects of particle morphology when the Reynolds number is constant.

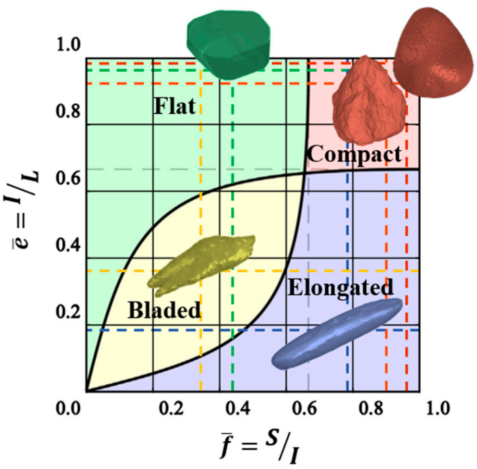

Figure 2. The five candidate particles presented in the particle classification system proposed by Angelidakis et al. [37] on a Zingg chart [36] (the dotted lines show the values of the two aspect ratios $\bar{e}$ and $\bar{f}$ for each particle with the corresponding colours).

2.2. Numerical Modelling of the Flow Around the Particle

For three-dimensional numerical modelling, the computational fluid domain is established as a rectangular cuboid with the particle positioned inside fixed on its place and experiencing an oncoming flow head-on with the dimensions and distances chosen based on the best practises of computational fluid dynamic modelling [38]. The boundary conditions needed for the numerical modelling are determined as a known velocity of 1 m/s at the inlet, resulting in the Reynolds number of 293.5 for all the particles since they are scaled to equate their length scales to $d = 4.29 \times 10^{-3}$ m, known ambient pressure at the outlet, and symmetry at the four sides of the rectangular cuboid. On the surface of the irregular particle, the no-slip boundary condition due to the viscosity of the fluid is imposed, which defines the fluid velocity near the wall equal to the velocity of the wall.

A mesh dependency analysis was performed to ensure that the computational grid is fine enough not to influence the results while also offering reasonable computational time resulting in a final computational mesh of ~140,000 tetrahedral elements (for more detail the readers are referred to [39]). The computational mesh is refined on and around the surface of all the particles to capture the intricate details of the flow corresponding to the particle's morphology as well as the irregularities on the particle surface.

The governing equations of motion for the fluid are the time-dependent continuity and Navier-Stokes equations:

$$\nabla.\left(\boldsymbol{U}_f\right) = 0 \tag{3}$$

$$\rho_f\left(\frac{\partial \boldsymbol{U}_f}{\partial t} + \left(\boldsymbol{U}_f \cdot \nabla\right)\boldsymbol{U}_f\right) = -\nabla P + \mu_f\left(\nabla^2 \boldsymbol{U}_f\right) \tag{4}$$

where t is the time and P is the fluid pressure [6]. The discretisation of the governing equations is performed using the Finite Volume Method (FVM). The Semi-Implicit Method for Pressure-Linked Equations (SIMPLE) is used to solve the equations with the convergence criteria of 10^{-6} and the time step of 10^{-6} s. Since the flow around an irregular object may create turbulence [38], Wall Adapting Local Eddy-Viscosity (WALE) model [40] is used for turbulence modelling, which as was shown in the literature produces the second least averaged absolute error [38]. A total number of 67 simulations including 8 for various orientations of the eight particle candidates and 4 for mesh dependency analysis is performed using the software ANSYS FLUENT 18.1.

2.3. Characteristics and Orientations of the Particle

Both compact particles are natural sand particles, the rounded one with the dimensions of $S = 0.0041$ m, $I = 0.0043$ m, $L = 0.0044$ m, and the surface area of $A_p = 6.09 \times 10^{-5}$ m^2, and the angular one with the dimensions of $S = 0.0044$ m, $I = 0.0049$ m, $L = 0.0052$ m, and the surface area of $A_p = 6.56 \times 10^{-5}$ m^2. Both particles are positioned at eight orientations with different sides facing the fluid flow and for each case, the drag coefficient is calculated through numerical simulation. Figures 3 and 4 show the eight orientations of the compact rounded and angular sand particles, respectively.

The flat particle is a recycled crushed glass granule [35] and has the dimensions of $S = 0.0023$ m, $I = 0.0052$ m, $L = 0.0053$ m, and the surface area of $A_p = 6.83 \times 10^{-5}$ m^2. Figure S1 in the Supplementary Information document presents the eight orientations of the flat RCG granule for which the drag coefficient is investigated. The elongated particle is a rice grain with the dimensions of $S = 0.0020$ m, $I = 0.0026$ m, $L = 0.0133$ m, and the surface area of $A_p = 8.55 \times 10^{-5}$ m^2. Figure S2 in the Supplementary Information document shows the eight orientations of the elongated rice grain for which the drag coefficient is studied. And finally, the bladed particle is an RCG granule which has the dimensions of $S = 0.0018$ m, $I = 0.008$ m, $L = 0.0124$ m, and the surface area of

$A_p = 10.03 \times 10^{-5}$ m^2. Its eight investigated orientations are presented in Figure S3 in the Supplementary Information document.

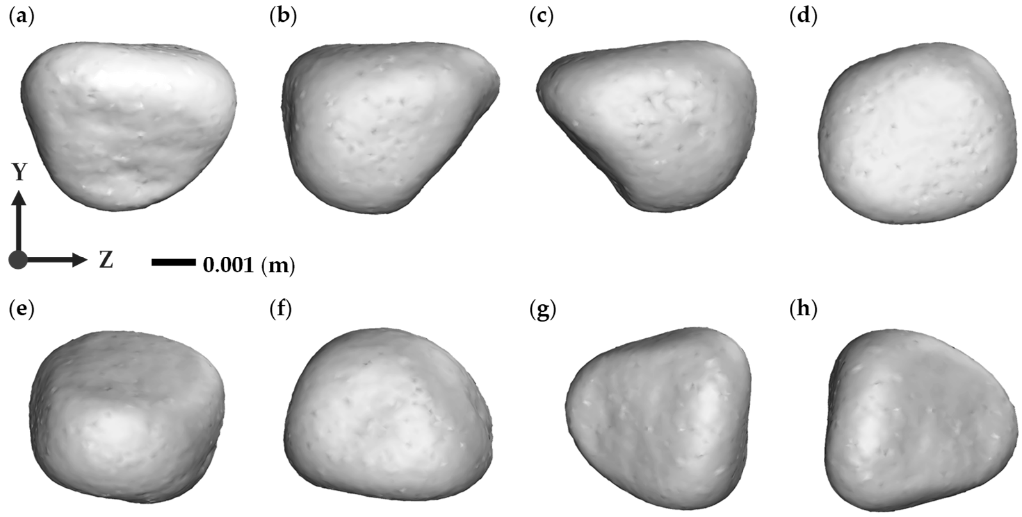

Figure 3. Compact rounded particle positioned at orientation (**a**) 1, (**b**) 2, (**c**) 3, (**d**) 4, (**e**) 5, (**f**) 6, (**g**) 7, and (**h**) 8.

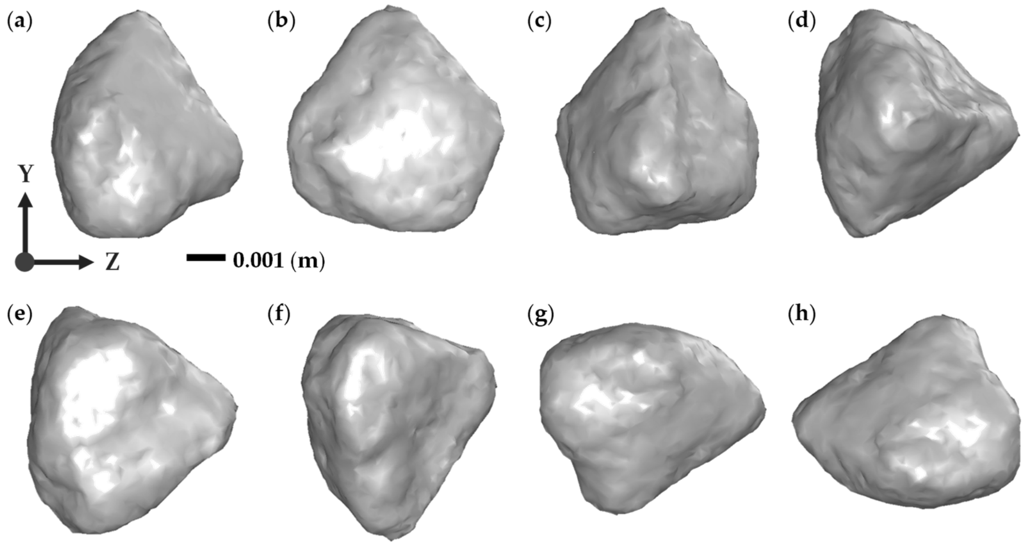

Figure 4. Compact angular particle positioned at orientation (**a**) 1, (**b**) 2, (**c**) 3, (**d**) 4, (**e**) 5, (**f**) 6, (**g**) 7, and (**h**) 8.

2.4. Empirical Drag Coefficient Models

Fourteen empirical models which use various particle morphology descriptors are chosen to estimate the drag coefficient of the irregular particles [8–11,13–19]. The results are compared to the data obtained from the numerical simulations. The formulation for all the fourteen drag models used in this research are presented in Table 1.

These empirical drag models are mainly developed for particles falling through a static fluid and explicitly depend on the Reynolds number, which itself depends on the size and settling velocity of the particle as well as the properties of the fluid. The drag coefficient equation for each of these empirical drag models can be iteratively solved using a guessed value for the initial Reynolds number, estimating the drag coefficient using the Reynolds number value, estimating the settling velocity using the drag coefficient value, and updating the Reynolds number using the estimated settling velocity value. This process is repeated until the difference between the updated Reynolds number and the

Reynolds number of the previous step becomes less than a user-specified criteria [8,19], which for the current work is set to 10^{-6}.

Table 1. Empirical drag models.

Drag Model	Shape Descriptors	Drag Coefficient
Bagheri and Bonadonna [8]	$\bar{e}$ $\bar{f}$	$C_D = \frac{24K_S}{Re}\left[1 + 0.125\left({}^{ReK_N}/_{K_S}\right)^{2/3}\right] + \frac{0.46K_N}{1+\frac{5330}{ReK_N/K_S}}$ $F_N = \bar{f}^2 \times \bar{e}\left(\frac{{d_{sph}}^3}{L\times i\times S}\right)\ K_N = 10^{\alpha_2(-logF_N)^{\beta_2}}$ $F_S = \bar{f} \times \bar{e}^{1.3}\left(\frac{{d_{sph}}^3}{L\times I\times S}\right)\ K_S = \frac{{F_S}^{1/3}+{F_S}^{-1/3}}{2}$ $\alpha_2 = 0.45 + 10/\left(exp\left(2.5\log{}^{\rho_p}/_{\rho_f}\right) + 30\right)$ $\beta_2 = 1 - 37/\left(exp\left(3\log{}^{\rho_p}/_{\rho_f}\right) + 100\right)$
Haider and Levenspiel [9]	Φ_W	$C_D = \frac{24}{Re}\left(1 + C_1 Re^{C_2}\right) + \frac{C_3}{1+{}^{C_4}/_{Re}}$ $C_1 = exp\left(2.33 - 6.46\Phi_W + 2.45{\Phi_W}^2\right)$ $C_2 = 0.096 + 0.556\Phi_W$ $C_3 = exp\left(4.09 - 13.89\Phi_W + 18.42{\Phi_W}^2 - 10.26{\Phi_W}^3\right)$ $C_2 = exp\left(1.47 + 12.26\Phi_W - 20.73{\Phi_W}^2 + 15.89{\Phi_W}^3\right)$
Ganser [10]	Φ_W	$C_D = \frac{24K_S}{Re}\left(1 + 0.1118\left({}^{ReK_N}/_{K_S}\right)^{0.6567}\right) + \frac{0.4305K_N}{\left(1+\frac{3305}{\left({}^{ReK_N}/_{K_S}\right)}\right)}$ $K_N = 10^{1.8148(-log\Phi_W)^{0.5743}}$ $K_S = {}^1/_3 + \left({}^2/_3\right)\sqrt{\Phi_W}$
Ganser [10] and Leith [11]	Φ_W $\Phi_\perp$	$C_D = \frac{24K_S}{Re}\left(1 + 0.1118\left({}^{ReK_N}/_{K_S}\right)^{0.6567}\right) + \frac{0.4305K_N}{\left(1+\frac{3305}{\left({}^{ReK_N}/_{K_S}\right)}\right)}$ $K_N = 10^{1.8148(-log\Phi_W)^{0.5743}}$ $K_S = {}^1/_3\sqrt{\Phi_\perp + \left({}^2/_3\right)\sqrt{\Phi_W}}$
Hölzer and Sommerfeld [12]	Φ_W $\Phi_\parallel$ $\Phi_\perp$	$C_D = \frac{8}{Re\sqrt{\Phi_\parallel}} + \frac{16}{Re\sqrt{\Phi_W}} + \frac{3}{\sqrt{Re}\sqrt[4]{{\Phi_W}^3}} + 0.42\left(10^{\left(0.4\left((-\log\Phi_W)^{0.2}/\Phi_\perp\right)\right)}\right)$
Tran-Cong et al. [13]	X_{surf}	$C_D = \frac{24}{\left(\frac{d_{surfsph}}{d_{sph}}Re\right)}\left(1 + \frac{0.15}{\sqrt{X_{surf}}}\left(\frac{d_{surfsph}}{d_{sph}}Re\right)^{0.687}\right) + \frac{0.42}{\sqrt{X_{surf}}\left[1+42{,}500\left(\frac{d_{surfsph}}{d_{sph}}Re\right)^{-1.16}\right]}$
Swamee and Ojha [14]	Φ_C Crushed Rock Fragments	$C_D = \left[\frac{48.5}{\left(1+4.5{\Phi_C}^{0.35}\right)^{0.8}Re^{0.64}} + \left(\frac{Re}{Re+100+1000\Phi_C}\right)^{0.32}\frac{1}{\left({\Phi_C}^{18}+1.05{\Phi_C}^{0.8}\right)}\right]^{1.25}$
	Φ_C Natural Sediments	$C_D = 0.84\left[\frac{333.78}{\left(1+4.5{\Phi_C}^{0.35}\right)^{0.8}Re^{0.56}} + \left(\frac{Re}{Re+700+1000\Phi_C}\right)^{0.28}\frac{1}{\left({\Phi_C}^{4}+20{\Phi_C}^{20}\right)^{0.175}}\right]^{1.428}$
Camenen [15]	Φ_C P	$C_D = \left[\left({}^{C_1}/_{C_2}\right)^{1/C_3} + {C_2}^{1/C_3}\right]^{C_3}$ $C_1 = 24 + 100\left[1 - \sin\left(\left({}^{\pi}/_2\right)\Phi_C\right)\right]^{2.1+0.06P}$ $C_2 = 0.39 + 0.22(6 - P) + 20\left[1 - \sin\left(\left({}^{\pi}/_2\right)\Phi_C\right)\right]^{1.75+0.35P}$ $C_3 = (1.2 + 0.12\text{P})\left[\sin\left(\left({}^{\pi}/_2\right)\Phi_C\right)\right]^{0.47}$

Table 1. *Cont.*

Drag Model	Shape Descriptors	Drag Coefficient
Wu and Wang [16]	Φ_C	$C_D = \left[\left(C_1 / Re \right)^{1/C_3} + C_2^{1/C_3} \right]^{C_3}$ $C_1 = 53.5e^{-0.65\Phi_C}$ $\quad C_2 = 5.65e^{-2.5\Phi_C}$ $\quad C_3 = 0.7 + 0.9\Phi_C$
Wang et al. [17]	Ψ	$C_D = 0.945 \frac{C_{D,sph}}{\Psi^{(0.641Re^{0.153})}} Re^{-0.01}$
Dioguardi and Mele [18]	Ψ	$C_D = \frac{C_{D,sph}}{Re^2 \Psi^{Re^{0.05}}} \left(\frac{Re}{1.1883} \right)^{1/0.4826} + \frac{0.42}{\sqrt{\Psi_{surf}} \left[1+42{,}500 \left(\frac{d_{surfsph}}{d_{sph}} Re \right)^{-1.16} \right]}$
Dioguardi et al. [19]	Ψ	$C_D = \frac{24}{Re} \left(\frac{1-\Psi}{Re} + 1 \right)^{0.25} + \frac{24}{Re} \left(0.1806 Re^{0.6459} \right) \Psi^{-Re^{0.08}} + \frac{0.4251}{1 + \frac{6880.95}{Re} \Psi^{Re^{5.05}}}$
Chien [20]	Φ_W	$C_D = \frac{30}{Re} + \left(\frac{67.289}{exp(5.03\Phi_W)} \right)$

Table 2 presents the particle morphology descriptors used in the drag models. The empirical models proposed by Chien [20], Ganser [10], Ganser and Leith [11], Haider and Levenspiel [9], and Hölzer and Sommerfeld [12] use the particle's true sphericity also known as Wadell's sphericity [34]. The models by Camenen [15], Swamee and Ojha [14], and Wu and Wang [16] use Corey's sphericity [41], and the models by Dioguardi and Mele [18], Dioguardi et al. [19], and Wang et al. [17] use the shape factor proposed by Dellino [42].

Table 2. Particle morphology descriptors.

Shape Descriptor	Formula	Description
$\bar{f}$	$\bar{f} = \frac{S}{I}$	Ratio of particle's minimum dimension (S) to intermediate dimension (I)
$\bar{e}$	$\bar{e} = \frac{I}{L}$	Ratio of particle's intermediate dimension (I) to maximum dimension (L)
Circularity [43]	$X = \frac{P_{mp}}{P_c}$	Ratio of maximum projection perimeter (P_{mp}) to perimeter of the circle equivalent (P_c) to the particle maximum projection area (A_{mp})
Surface Circularity [13]	$X_{surf} = \frac{\pi d_{surfsph}}{P_{mp}}$	Ratio of perimeter of the surface area equivalent sphere ($\pi d_{surfsph}$) to maximum projection perimeter (P_{mp}).
Particle (true) Sphericity by Wadell [34]	$\Phi_W = \frac{A_{sph}}{A_p}$	A measure of how spherical an object is; Ratio of surface area of the volume equivalent sphere (A_{sph}) to particle surface area (A_p)
Particle Sphericity by Krumbein [44]	$\Phi_K = \sqrt[3]{\frac{S \times I}{L^2}}$	A measure of how spherical an object is
Particle Sphericity by Corey [41]	$\Phi_C = \frac{S}{\sqrt{L \times I}}$	A measure of how spherical an object is
Lengthwise Sphericity [12]	$\Phi_{\parallel}$	Ratio of the cross-sectional area of the volume equivalent sphere and the difference between half the surface area to the mean projected cross-sectional area of the particle parallel to flow
Crosswise sphericity [12]	$\Phi_{\perp}$	Ratio of the cross-sectional area of the volume equivalent sphere to the projected cross-sectional area of the particle
Roundness [45]	$P = \frac{r}{R_{in}}$	A measure of how spherical an object is
Shape Factor by Dellino [42]	$\Psi = \frac{\Phi_W}{X}$	Ratio of true sphericity [40] to circularity [43]

3. Results and Discussions

3.1. Regular Ellipsoidal Particles

The focus of our previous research was on investigating the drag force on ellipsoidal particles with various aspect ratios (as defined in Angelidakis et al. [37]) operating in the intermediate flow regime [8] with $137 \leq Re \leq 234$ through CFD [39]. It was shown that the models by Haider and Levenspiel [9], Ganser [10], and Leith [11] can be appropriate choices for the particles belonging to all four morphological categories. Additionally, for the ellipsoids in the compact region of the Zingg chart [36], most of the models (except the one by Tran-Cong et al. [13]) proved suitable. The models proposed by Wang et al. [17], Dioguardi and Mele [18], Dioguardi et al. [19], Swamee and Ojha [14], and Wu and Wang [16] were confirmed to be capable of estimating the drag coefficient for ellipsoids belonging to the bladed and elongated categories of the Zingg chart [36]. For ellipsoidal particles in the flat region of the Zingg chart [36], the models by Bagheri and Bonadonna [8] and Tran-Cong et al. [13] proved to be efficient.

In the current work, the nine most used drag coefficient models based on our literature review (Figure 1b) are used to estimate the drag coefficient of ellipsoidal particles with various aspect ratios shown in Figure 5a. The results are presented on a Zingg chart [36] using the classification system proposed by Angelidakis et al. [37] and shown in Figure 5(c-1)–(l-1). The values of the drag coefficient estimated using the nine drag models are then compared to the data obtained from the CFD simulations, which are shown in Figure 5b and the corresponding error percentages are presented in Figure 5(c-2)–(l-2).

If the accuracy of the drag models is defined as a desired percentage difference between the drag model and the numerical simulation, a criterion for the particles' aspect ratio i.e., ranges of I/L and S/I can be identified for each drag model to result in an estimation of the drag coefficient with the desirable accuracy. For example, an accuracy of 25% difference with the numerical simulation results in the below criteria for each drag model:

- The model by Hölzer and Sommerfeld [12] presents accurate data for compact ellipsoids with their $I/L + 0.5S/I \gtrsim 1.3$.
- The model by Haider and Levenspiel [9] presents accurate data for flat and bladed ellipsoids with their $S/I \lesssim 0.5$ or compact ellipsoids with their $I/L + S/I \gtrsim 1.9$.
- The model by Ganser [10] presents accurate data for flat and bladed ellipsoids with their $S/I \lesssim 0.4$ or compact ellipsoids with their $I/L + S/I \gtrsim 1.9$.
- The model by Wang et al. [17] presents accurate data for elongated and bladed ellipsoids with their $I/L \lesssim 0.3$.
- The model by Chien [20] presents accurate data for elongated and bladed ellipsoids with their $I/L \gtrsim 0.4$ and $I/L + 1.5S/I \lesssim 1.1$ or compact ellipsoids with their $I/L + S/I \gtrsim 1.9$.
- The model by Bagheri and Bonadonna [8] presents accurate data for compact and flat ellipsoids with their $I/L - 0.333S/I \gtrsim 0.767$.
- The model by Swamee and Ojha [14] presents accurate data for compact and elongated ellipsoids with their $I/L - S/I \lesssim -0.2$ for crushed rock fragments, and $I/L - S/I \lesssim 0$ for natural sediments.
- The model by Dioguardi et al. [19] presents accurate data for elongated and bladed ellipsoids with their $I/L \lesssim 0.3$ or compact ellipsoids with their $I/L + S/I \gtrsim 1.9$.
- The model by Tran-Cong et al. [13] presents accurate data for flat, elongated, and bladed ellipsoids with their $I/L + 0.375S/I \gtrsim 0.775$.

For a difference of less than either 10%, 20%, or 30% with the numerical simulation, the above nine models can estimate the drag coefficient of ellipsoidal particles with a wide range of I/L and S/I values, which covers a defined area of the Zingg chart as shown in Figure 6a to c, respectively. If a difference of more than 40% is acceptable, the model proposed by Ganser [10] covers the whole Zingg chart by itself. Additionally, a combination of other models can be suitable.

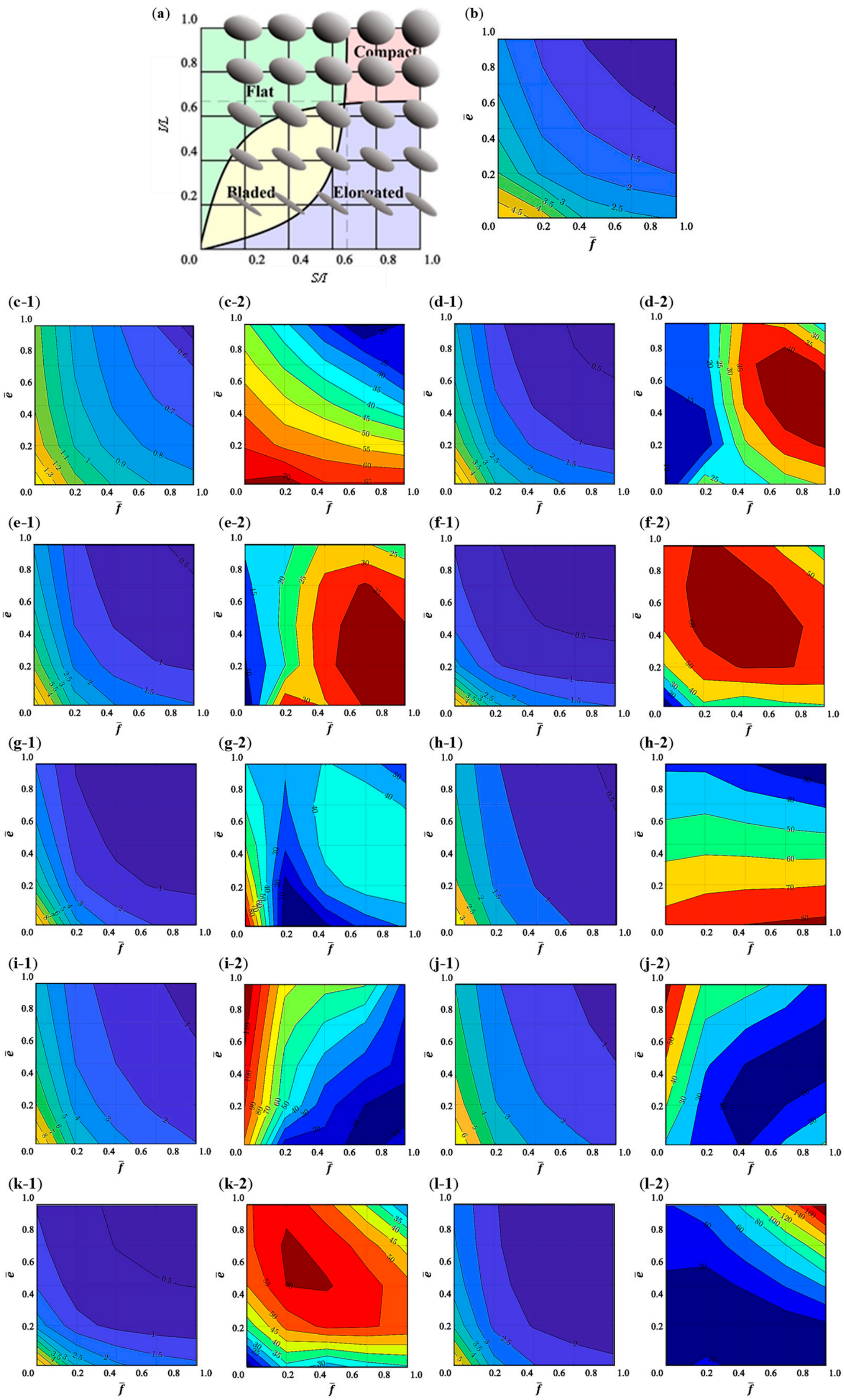

Figure 5. (**a**) Ellipsoids with varying aspect ratios, the (**b**) drag coefficient obtained from CFD, (**1**) drag coefficient estimated using the model by (**c**) Hölzer and Sommerfeld [12], (**d**) Haider and Levenspiel [9,39], (**e**) Ganser [10,39], (**f**) Wang et al. [17,39], (**g**) Chien [20], (**h**) Bagheri and Bonadonna [8,39], (**i**) Swamee and Ojha (crushed rock fragments) [14,39], (**j**) Swamee and Ojha (natural sediments) [14,39], (**k**) Dioguardi et al. [19,39], and (**l**) Tran-Cong et al. [13,39], and (**2**) their corresponding error percent compared to CFD presented on Zingg charts using the classification system proposed by Angelidakis et al. [37].

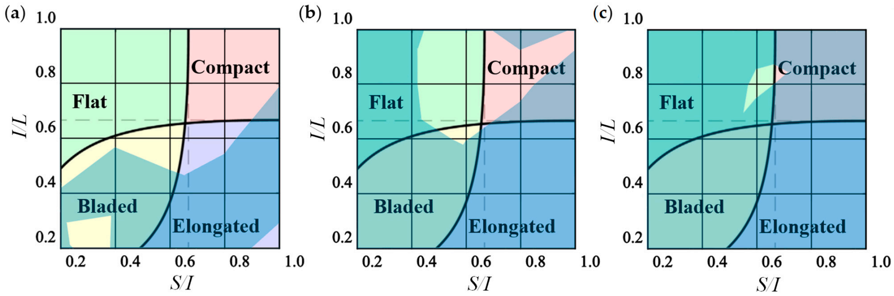

Figure 6. The shaded area on the Zingg chart shows the coverage of the drag models for which at least one of the nine drag models are accurate in estimating the drag coefficient for ellipsoids with varying aspect ratios with an accuracy of (**a**) 10%, (**b**) 20%, and (**c**) 30% relative to the numerical simulation.

3.2. Irregular Particles: Compact Morphologies

Compact particles with their morphology closest to actual spheres can be commonly encountered in nature. Here, two different compact particles positioned at eight different orientations are chosen to investigate the drag they experience and determine the most suitable empirical model to estimate the drag coefficient of compact particles. Table S1 in the Supplementary Information document presents the drag force, particle area facing the flow, and the drag coefficient obtained from numerical simulation for each compact particle at the eight orientations. The drag coefficient is proportional to the ratio of the drag force to the area facing the flow and thus for the rounded compact particle, orientations 4 and 3, and for the angular compact particle, orientations 2 and 4 result in the minimum and maximum drag coefficient values, respectively.

The average value of the drag coefficient over all eight orientations is 1.53 for the rounded and 1.57 for the angular compact particle. Figure 7 summarises the drag coefficient values for both compact particles positioned at the eight orientations. For compact particles, the difference between the maximum and minimum values of the drag coefficient is not significant with percentages of 11.4% and 12.6% for the rounded and angular compact particles, respectively.

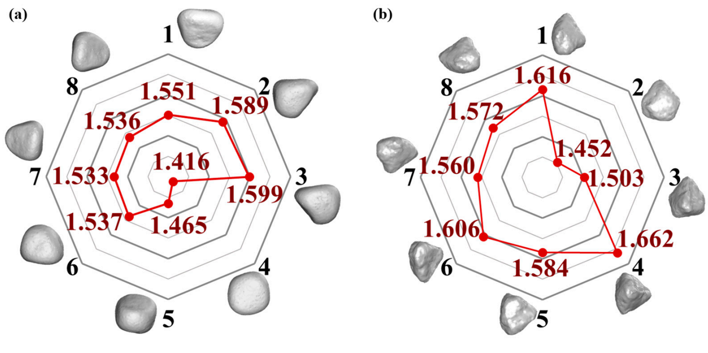

Figure 7. Comparison of the drag coefficient values for the compact (**a**) rounded, and (**b**) angular particle positioned at the eight different orientations facing the fluid flow.

For each particle morphology, the maximum ($C_{D\,max}$) and minimum ($C_{D\,min}$) values of the drag coefficient correspond to the minimum (A_{min}) and the maximum (A_{max}) projected areas, respectively. Tagliavini et al. [38] proposed that particles' drag coefficient can be estimated with reasonable accuracy using the harmonic mean of the minimum and maximum values of the drag coefficients:

$$\tilde{C_D} = \frac{2C_{D\,min}C_{D\,max}}{C_{D\,min} + C_{D\,max}} \tag{5}$$

where $\widetilde{C_D}$ represents the estimated value of the particles' drag coefficient. For the rounded and the angular compact particle, $\widetilde{C_D}$ equals to 1.50 and 1.55, respectively.

Fourteen empirical drag models were used to calculate the drag coefficient of the compact particles and the values along with the error corresponding to the average drag coefficient obtained from CFD are presented in Table 3. Among these fourteen empirical models, only the ones proposed by Hölzer and Sommerfeld [12], Ganser [10] and Leith [11], and Tran-Cong et al. [13] account for the orientation of the particle. For each of these models the harmonic mean of the drag coefficients using the projected areas of minimum and maximum principal moments of inertia ($\widetilde{C_D}$) is calculated [38].

Table 3. Drag coefficient of the two compact particles obtained using the empirical drag models (the colours show the value of the error from darkest lowest error value to lightest highest error value).

	Rounded		Angular	
				
C_D from CFD Averaged over All orientations	1.528		1.569	
Drag Model	**C_D**	**Error (%)**	**C_D**	**Error (%)**
Bagheri and Bonadonna [8]	0.412	73.036	0.522	66.73
Camenen [15]	1.552	1.57	1.565	0.254
Chien [20]	0.582	61.91	0.814	48.119
Dioguardi and Mele [18]	0.574	62.434	0.691	55.959
Dioguardi et al. [19]	0.514	66.361	0.671	57.233
Ganser [10]	0.652	57.329	0.906	42.256
Ganser [10] and Leith [11]	0.653	57.264	0.908	42.128
Haider and Levenspiel [9]	0.568	62.827	0.875	44.231
Hölzer and Sommerfeld [12]	0.736	51.832	0.828	47.227
Swamee and Ojha [14] Natural Sediments	0.589	61.452	0.728	53.601
Swamee and Ojha [14] Crushed Rock Fragments	0.758	50.392	0.941	40.025
Tran-Cong et al. [13]	1.707	11.714	1.898	20.968
Wang et al. [17]	0.435	71.531	0.574	63.416
Wu and Wang [16]	0.621	59.358	0.698	55.513

For these compact particles, the models proposed by Camenen [15] and Tran-Cong et al. [13] produce the lowest error values of ~2.5% and ~21%, respectively. All the other empirical drag models result in error values of over ~40% which shows their inability to accurately estimate the drag force of the compact particles. Comparing the findings of the current investigation regarding the compact particles to the conclusions of our previous study [39], the models suitable for compact ellipsoids (spheres and spheroids) are not necessarily suitable for compact irregular particles. This shows that drag models presenting more accurate predictions of the irregular compact particles' drag coefficient are in demand.

3.3. Irregular Particles: Flat and Elongated Morphologies

For the flat and the elongated particles positioned at the eight different orientations, their morphological category, drag force, area facing the flow, and drag coefficient obtained from numerical simulation are presented in Table S2 in the Supplementary Information document. For the flat particle, orientations 5 and 6 and for the elongated particle, Orientations 2 and 4 generate the minimum and maximum drag coefficient values, respectively.

The average value of the drag coefficient for all these eight orientations is 1.854 for the flat RCG granule and 2.678 for the elongated rice grain. The estimated value of the particles' drag coefficient, $\widetilde{C}_D$, using the harmonic mean of the maximum and minimum values of the drag coefficient equals to 1.77 for the flat and 2.42 for the elongated particle. Figure 8 summarises the drag coefficient values for the two particles positioned at the eight orientations. As expected, the effect of particle orientation on drag coefficient values is dramatic for elongated particles.

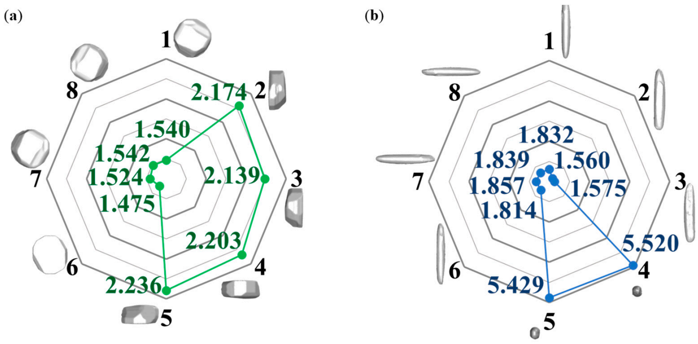

Figure 8. Comparison of the drag coefficient values for the (**a**) flat RCG granule and (**b**) elongated rice grain, positioned at the eight different orientations facing the fluid flow.

Table 4 presents values of the drag coefficient estimated using the fourteen empirical drag models as well as their difference compared to the average drag coefficient obtained from CFD for the flat and the elongated particles. Tables providing the comparison of the drag coefficient resulted from the fourteen empirical drag models to the drag coefficient of each particle orientation is presented in the Supplementary Information document.

Table 4. Drag coefficient of the flat and the elongated particles obtained using the empirical drag models (the colours show the value of the error from darkest lowest error value to lightest highest error value).

	Flat		**Elongated**	
	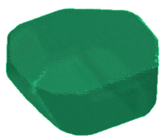		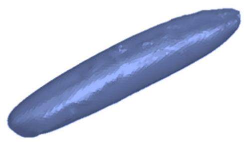	
C_D from CFD Averaged over All orientations	**1.854**		**2.678**	
Drag Model	**C_D**	**Error (%)**	**C_D**	**Error (%)**
Bagheri and Bonadonna [8]	0.763	58.845	0.976	63.554
Camenen [15]	3.095	66.936	3.714	38.685
Chien [20]	0.97	47.68	2.272	15.16
Dioguardi and Mele [18]	0.673	63.7	1.65	38.386
Dioguardi et al. [19]	0.647	65.102	1.833	31.553
Ganser [10]	1.049	43.419	1.955	26.997
Ganser [10] and Leith [11]	1.05	43.365	1.937	27.669
Haider and Levenspiel [9]	1.068	42.394	2.136	20.238
Hölzer and Sommerfeld [12]	0.847	54.314	0.871	67.475
Swamee and Ojha [14] Natural Sediments	1.817	1.995	2.262	15.533
Swamee and Ojha [14] Crushed Rock Fragments	2.079	12.135	2.624	2.016
Tran-Cong et al. [13]	1.951	5.231	2.291	14.451
Wang et al. [17]	0.552	70.226	1.904	28.902
Wu and Wang [16]	1.911	3.074	2.384	10.978

The model presented by Swamee and Ojha [14] for natural sediments and crushed rock fragments results in a minimum error of ~2% for flat and elongated particles, respectively. This is consistent with our previous study in which the model proposed by Swamee and Ojha [14] showed promise for elongated ellipsoidal particles [39]. The next drag coefficient model appropriate for flat and elongated particles, is the models by Wu and Wang [16] with a ~3% and ~11% error, respectively. The model proposed by Tran-Cong et al. [13] can be the third option for estimating the drag force of the flat and elongated particles with an error of ~5% and ~14% error, respectively.

An interesting observation that can be made here is that the same empirical drag models are accurate in their estimation of the drag coefficient for both the flat and elongated particles. This may be due to existence of high percentages of flat and elongated particles among the experimental data used to formulate these empirical models.

3.4. Irregular Particles: Bladed Morphologies

The drag force, particle area facing the flow, and the drag coefficient obtained from numerical simulation are presented in Table S2 in the Supplementary Information document for the bladed particle. Orientations 2 and 4 result in the minimum and maximum drag coefficient values, respectively, for the Bladed RCG granule. The average value of the drag coefficient for all eight orientations is 2.605 and the estimated value of the particles' drag coefficient, $\widetilde{C_D}$, using the harmonic mean of the maximum and minimum values of the drag coefficient is 2.49 for the RCG granule. Figure 9 summarises the drag coefficient values for the bladed particle positioned at the eight orientations showing the dramatic effect of particle orientation on drag coefficient values.

The values of the drag coefficient estimated using the fourteen empirical drag models as well as their difference compared to the average drag coefficient obtained from CFD is presented in Table 5. Tables providing the comparison of the drag coefficient resulted from the fourteen empirical drag models to the drag coefficient of each particle orientation is presented in the Supplementary Information document.

For the bladed particle, the models proposed by Ganser [10] and Leith [11] show a minimum error of ~11% and this reaffirms our previous conclusions for bladed ellipsoidal particles [39]. The next lowest error with a value of ~15% belongs to the model by Haider and Levenspiel [9]. There is a low chance of encountering high percentages of bladed particles in nature, so the performance of these empirical drag models seems reasonable.

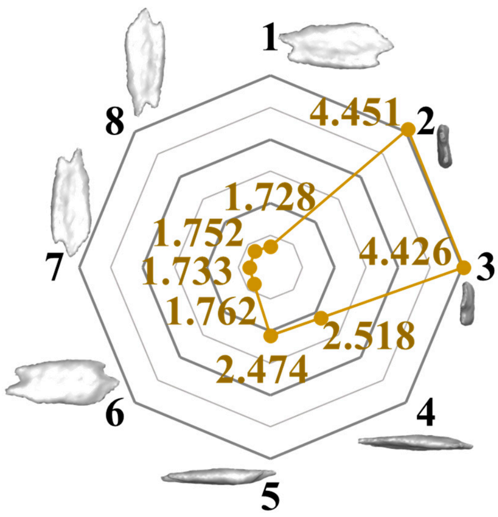

Figure 9. Comparison of the drag coefficient values for the bladed RCG granule, positioned at the eight different orientations facing the fluid flow.

Table 5. Drag coefficient of the bladed particle obtained using the empirical drag models (the colours show the value of the error from darkest lowest error value to lightest highest error value).

Bladed		
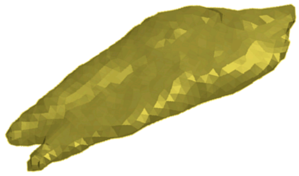		
C_D from CFD Averaged over All orientations	**2.605**	
Drag Model	**C_D**	**Error (%)**
Bagheri and Bonadonna [8]	1.784	31.516
Camenen [15]	6.476	148.598
Chien [20]	4.025	54.51
Dioguardi and Mele [18]	1.829	29.788
Dioguardi et al. [19]	2.05	21.305
Ganser [10]	2.91	11.708
Ganser [10] and Leith [11]	2.907	11.593
Haider and Levenspiel [9]	2.995	14.971
Hölzer and Sommerfeld [12]	1.131	56.583
Swamee and Ojha [14] Natural Sediments	3.396	30.364
Swamee and Ojha [14] Crushed Rock Fragments	4.05	55.47
Tran-Cong et al. [13]	3.19	22.456
Wang et al. [17]	2.175	16.506
Wu and Wang [16]	3.224	23.761

3.5. Approximating the Particle Drag by Single Sphere Representations

Aside from CFD and empirical drag models, another approach to estimate particles' drag coefficient is to represent them by a single sphere. According to our literature review, this is a popular approach for modelling the drag force especially in coupled CFD-DEM simulations.

When the morphology of a particle is simplified to a sphere, the size of the sphere can be chosen based on the particle's morphological characteristics. These choices can include the volume equivalent sphere, the surface area equivalent sphere, the inscribed sphere, and the circumscribed sphere. This approach may be more appropriate for compact particles compared to the other three categories due to the particle morphologies being more similar to actual spheres.

Here, the angular compact particle is represented by spheres of various sizes chosen based on the particles' morphological characteristics. The resulting drag coefficient of these spherical representations is as follows: 1.024 for the volume equivalent sphere with a 34.73% difference, 0.974 for the surface area equivalent sphere with a 37.94% difference, 1.472 for the inscribed sphere with a 6.19% difference, and 0.878 for the circumscribed sphere with a 44.05% difference compared to the CFD data for the actual morphology. Therefore, in this case, the inscribed sphere is the most suitable for estimating the drag force of the compact particles.

The single sphere representation of the flat RCG granule results in the estimated drag coefficients for each spherical representation to be: 1.024 for the volume equivalent sphere with a 44.76% difference, 0.951 for the surface area equivalent sphere with a 48.71% difference, 1.609 for the inscribed sphere with a 13.23% difference, and 0.852 for the circumscribed sphere with a 54.07% difference compared to the CFD data for the actual morphology. Given the above data, single sphere representations can be appropriate for flat particles with higher sphericities.

The single sphere representation is not a viable option for elongated and bladed particles with a minimum difference of ~39% and ~35% calculated compared to the CFD results for their corresponding inscribed spheres, respectively. More complex particle morphologies can also be represented as clumps of more than one spherical elements especially for classic DEM modelling. In this approach, a compromise between the accuracy of shape representation and the cost of the numerical modelling should be made [3].

3.6. Aerodynamic Properties of Irregular Particles

Figure 10 shows the pressure and velocity fields around four irregular particles positioned at the orientations which results in the minimum and maximum value of the drag coefficient. For the cases with minimum drag coefficient, the stagnation region (area with maximum pressure and minimum near zero velocity) is larger while for the cases with maximum drag coefficient, the stagnation region is smaller. Between all the investigated orientations for each particle, the orientation with the bluntest surface area facing the flow results in the minimum and the orientation with the sharpest surface area facing the flow results in the maximum drag coefficient.

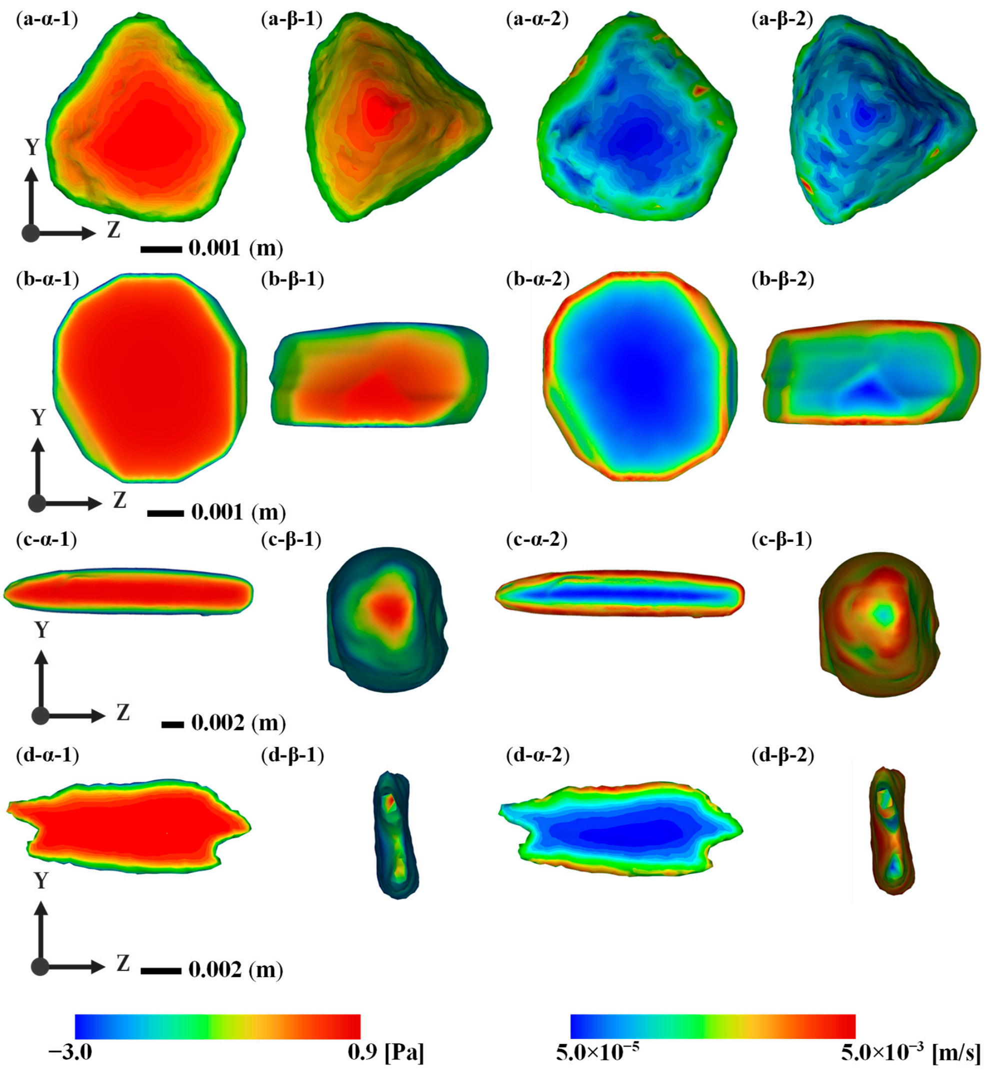

Figure 10. The fields of (**1**) pressure and (**2**) velocity around the (**a**) compact angular particle, (**b**) flat RCG granule, (**c**) elongated rice grain, and (**d**) bladed RCG granule for the (**α**) minimum, and (**β**) maximum drag coefficient.

3.7. Drag Model Accuracy over a Range of the Reynolds Number

In the previous sections, the drag coefficient of irregular particles has been investigated for a constant value of the Reynolds number. To assess whether the proposed empirical drag models for each particle morphology can be generalised across a range of Reynolds numbers, a study focusing on two factors—Reynolds number and particle morphology—is conducted.

As presented in Figure 11, all fourteen drag models are claimed to be operational in the range of Reynolds number values $1 \leq Re \leq 1500$, thus Reynolds numbers with four orders of magnitude, namely, O(1), O(10), O(100), and O(1000) are studied. The Reynolds number equal to 293.5 with the order of magnitude of O(100) has already been investigated in the previous sections for all particle morphologies. Since the iterative approach of estimating the drag coefficient uses the value of the particle's settling velocity to calculate the Reynolds number, the particle size is the only other particle related variable that changes the Reynolds number.

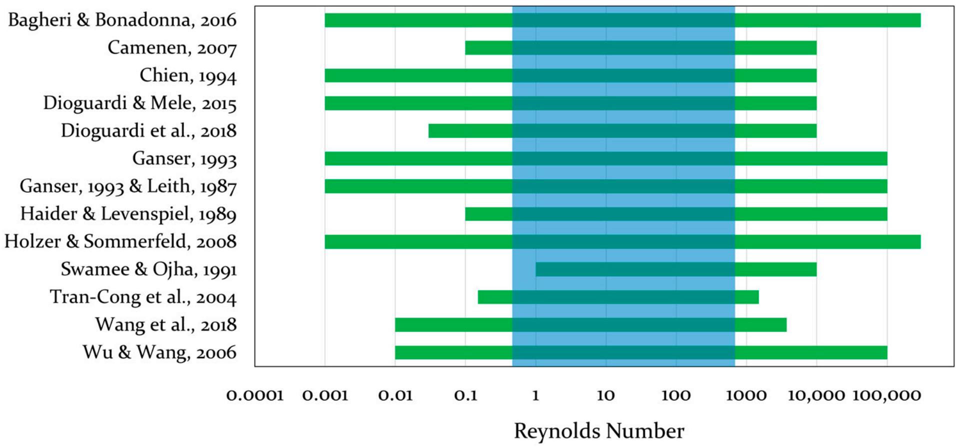

Figure 11. The range of the Reynolds number each empirical drag coefficient models operates at [8–20] (shown in green) and the range of Reynolds number between 1 and 1500 considered in this study (shown in blue).

Among the four particle morphology categories, only the compact, flat, and elongated particles are examined here, neglecting the bladed particles since there is low chance of encountering natural bladed particles in many applications.

For the five values of the Reynolds number and the three particle morphologies the full factorial Design of eXperiment (DoX) method requires all the possible 15 cases to be examined; all of which need to be modelled twice by positioning the particle at the two orientations resulting in the maximum and the minimum values of drag coefficient needed for the calculation of $\widetilde{C_D}$.

To reduce the number of the numerical simulations while preserving the accuracy of the statistical analysis the fractional factorial DoX is used. A study with two factors, namely, Reynolds number and particle morphology, the former comprising five levels of 2.94, 58.7, 146.75, 586.98, and 1467.47, and the latter having three levels of compact, flat, and elongated is considered. A fractional factorial design of 11 case studies is investigated. The particle morphologies chosen for these 11 case studies are unlike the five particles studied in the previous sections and are shown in Figure 12. For each case study, two simulations are performed to obtain the maximum and the minimum values of drag coefficient so the $\widetilde{C_D}$ can be calculated. This results in the total number of 22 simulations.

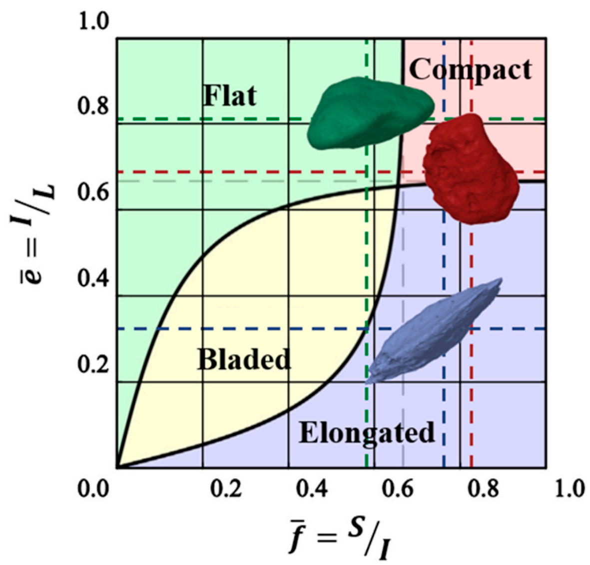

Figure 12. The three candidate particles for the Reynolds Number study presented in the particle classification system proposed by Angelidakis et al. [36] on a Zingg chart [35] (the dotted lines show the values of the two aspect ratios $\bar{e}$ and $\bar{f}$ for each particle with the corresponding colours).

Tables 6–8 present the values of the estimated drag coefficient ($\widetilde{C}_D$) obtained through CFD, the drag coefficients obtained from the fourteen empirical drag models, and the difference between the two. As previously stated, only the models proposed by Hölzer and Sommerfeld [12], Ganser [10] and Leith [11], and Tran-Cong et al. [13] account for the orientation of the particle for which the harmonic mean of the drag coefficients ($\widetilde{C}_D$) is presented.

Table 6. Drag coefficient of the fractional factorial DoX case studies for the compact particle obtained using the empirical drag models (the colours show the value of the error from darkest lowest error value to lightest highest error value).

Reynolds Number	**2.94**		**58.7**		**586.98**		**1467.47**	
Particle Morphology	**Compact**		**Compact**		**Compact**		**Compact**	
$\widetilde{C}_D$ from CFD	**145.75**		**7.240**		**0.920**		**0.628**	
Drag Model	**C_D**	**Error (%)**	**C_D**	**Error (%)**	**C_D**	**Error (%)**	**C_D**	**Error (%)**
Bagheri and Bonadonna [8]	143.65	1.439	0.875	87.919	0.737	19.912	0.814	29.557
Camenen [15]	154.68	6.129	2.519	65.209	2.176	136.487	2.164	244.709
Chien [20]	189.17	29.80	1.114	84.617	0.957	3.98	0.954	51.859
Dioguardi and Mele [18]	86.80	40.443	1.218	83.171	0.796	13.479	1.043	66.138
Dioguardi et al. [19]	211.99	45.45	1.205	83.359	0.661	28.148	0.606	3.494
Ganser [10]	123.73	15.105	1.061	85.342	1.145	24.395	1.185	88.703
Ganser [10] and Leith [11]	117.98	19.05	1.054	85.45	1.146	24.581	1.185	88.7
Haider and Levenspiel [9]	143.86	1.292	0.965	86.664	1.144	24.347	1.172	86.614
Hölzer and Sommerfeld [12]	159.46	9.408	1.192	83.539	0.837	8.997	0.814	29.641
Swamee and Ojha [14] Natural Sediments	84.64	41.93	1.359	81.233	1.371	48.981	1.386	120.833
Swamee and Ojha [14] Crushed Rock Fragments	84.15	42.26	1.454	79.917	1.527	65.923	1.538	144.988
Tran-Cong et al. [13]	627.50	330.54	4.034	44.28	2.128	131.266	2.470	293.441
Wang et al. [17]	157.07	7.77	1.088	84.972	0.676	26.544	0.893	42.242
Wu and Wang [16]	276.35	89.62	1.633	77.446	1.234	34.059	1.218	94.029

Table 7. Drag coefficient of the fractional factorial DoX case studies for the flat particle obtained using the empirical drag models (the colours show the value of the error from darkest lowest error value to lightest highest error value).

Reynolds Number	**2.94**		**58.7**		**146.75**		**1467.47**	
Particle Morphology	**Flat**		**Flat**		**Flat**		**Flat**	
$\tilde{C}_D$ from CFD	**151.50**		**7.55**		**3.088**		**0.711**	
Drag Model	**C_D**	**Error (%)**	**C_D**	**Error (%)**	**C_D**	**Error (%)**	**C_D**	**Error (%)**
Bagheri and Bonadonna [8]	150.80	0.46	1.023	86.454	0.747	75.797	0.985	38.55
Camenen [15]	198.54	31.05	3.417	54.75	3.128	1.3	3.022	325.24
Chien [20]	189.29	24.94	1.174	84.45	1.048	66.061	1.010	42.05
Dioguardi and Mele [18]	93.59	38.22	1.307	82.691	0.859	72.17	1.117	57.16
Dioguardi et al. [19]	222.93	47.15	1.305	82.719	0.867	71.934	0.634	10.83
Ganser [10]	123.20	18.68	1.099	85.443	0.983	68.152	1.236	73.92
Ganser [10] and Leith [11]	118.62	21.7	1.094	85.509	0.985	68.106	1.236	73.91
Haider and Levenspiel [9]	144.77	4.44	1.004	86.712	1.005	67.456	1.233	73.48
Hölzer and Sommerfeld [12]	158.66	4.72	1.204	84.05	0.953	69.131	0.818	15.03
Swamee and Ojha [14] Natural Sediments	91.60	39.54	1.567	79.252	1.477	52.158	1.644	131.31
Swamee and Ojha [14] Crushed Rock Fragments	91.06	39.89	1.707	77.394	1.688	45.337	1.824	156.64
Tran-Cong et al. [13]	636.60	320.2	4.099	45.707	2.374	23.13	2.510	253.19
Wang et al. [17]	163.94	8.21	1.177	84.41	0.744	75.903	1.011	42.214
Wu and Wang [16]	310.70	105.09	1.956	74.099	1.658	46.29	1.547	117.62

Table 8. Drag coefficient of the fractional factorial DoX case studies for the elongated particle obtained using the empirical drag models (The colours show the value of the error from darkest lowest error value to lightest highest error value).

Reynolds Number	**2.935**		**58.699**		**1467.47**	
Particle Morphology	**Elongated**		**Elongated**		**Elongated**	
$\tilde{C}_D$ from CFD	**198.19**		**9.88**		**0.96**	
Drag Model	**C_D**	**Error (%)**	**C_D**	**Error (%)**	**C_D**	**Error (%)**
Bagheri and Bonadonna [8]	210.614	6.266	1.344	86.396	1.269	31.873
Camenen [15]	295.271	48.98	5.287	46.499	4.861	404.902
Chien [20]	191.945	3.153	2.596	73.732	2.351	144.236
Dioguardi and Mele [18]	203.422	2.637	2.709	72.585	2.249	133.636
Dioguardi et al. [19]	312.686	57.766	2.968	69.969	1.141	18.534
Ganser [10]	115.417	41.765	1.801	81.776	2.188	127.326
Ganser [10] and Leith [11]	118.095	40.414	1.813	81.648	2.189	127.341
Haider and Levenspiel [9]	166.709	15.886	1.876	81.015	2.236	132.262
Hölzer and Sommerfeld [12]	210.267	6.091	1.330	86.536	0.838	12.911
Swamee and Ojha [14] Natural Sediments	100.694	49.194	1.857	81.202	2.017	109.513
Swamee and Ojha [14] Crushed Rock Fragments	100.093	49.497	2.074	79.016	2.243	132.943
Tran-Cong et al. [13]	799.898	303.591	5.107	48.324	3.132	225.326
Wang et al. [17]	252.916	27.609	2.576	73.929	3.248	237.428
Wu and Wang [16]	350.028	76.607	2.361	76.109	1.968	104.457

From the data reported in Tables 6–8, it is evident that when the Reynolds number is equal to 2.94, for each of the three particle morphologies, as high as twelve of the fourteen empirical drag models offer reasonable accuracy, a difference of below 40% compared to CFD. For this low value of the Reynolds number only the drag coefficient models by Tran-Cong et al. [13] and Wu and Wang [16] immensely overestimate the value of the drag coefficient.

Increasing the Reynolds number to 58.7 and then 146.75 results in a dramatic decline in the accuracy for all the empirical drag models as their difference compared to CFD raises above 45% for all fourteen models. At these two values of the Reynolds number, all drag models underestimate the value of the particle drag coefficients for all three morphologies. The two drag coefficient models by Camenen [15] and Tran-Cong et al. [13] seem to result in the least difference compared to CFD.

As the Reynolds number reaches 586.98, the accuracy of the empirical drag models recovers with only four out of fourteen drag models resulting in differences of over 40% compared to CFD. At this Reynolds number, the drag coefficient models by Camenen [15] and Hölzer and Sommerfeld [12] are shown to be the most accurate models.

For the highest value of Reynolds number equal to 1467.47, only four empirical drag models offer reasonable accuracy of below 40% difference compared to CFD for all three particle morphologies with most of the drag models overestimating the value of the drag coefficient. The drag coefficient estimations using Dioguardi et al. [19] and Hölzer and Sommerfeld [12] drag coefficient models present the highest accuracy.

A summary of the above discussion is presented in Figure 13. It can be concluded that although all these fourteen drag models are claimed to be operational within a wide range of Reynolds numbers, most of them perform particularly better for the low values of the Reynolds number. A detailed examination of the performance of the empirical drag models over the range of Reynolds number $1 \leq Re \leq 1500$ is presented for a few selected models:

- The drag coefficient model by Camenen [15] offers high accuracy when the Reynolds number is lower within the order of magnitude of O(1) to O(100). However, for higher Reynolds number with order of magnitude of O(100) and O(1000), this model does not perform very well.
- The accuracy of the drag coefficient model by Tran-Cong et al. [13], while inadequate for low Reynolds numbers, start to increase when the Reynolds number increases to the order of magnitude of O(100). As the Reynolds number further increases towards the order of magnitude of O(1000), the accuracy of the model by Tran-Cong et al. [13] declines again.
- The drag coefficient model by Wu and Wang [16] shows a similar behaviour to model by Tran-Cong et al. [13] for most cases.
- The drag coefficient estimations of the two models by Swamee and Ojha [14] for natural sediments and crushed rock fragments decrease in accuracy as the Reynolds number increases.
- The accuracy of the drag coefficient model by Hölzer and Sommerfeld [12] is acceptably high for lowest and highest values of the Reynolds number with orders of magnitude of O(1) and O(1000), respectively. However, for the Reynolds numbers within the orders of magnitude of O(10) to O(100), the accuracy of this model is not acceptable.
- The drag coefficient model by Haider and Levenspiel [9] shows a similar behaviour to model by Hölzer and Sommerfeld [12] for most cases.

One noticeable observation in Figure 13 is that in the Reynolds number range of $50 \lesssim Re \lesssim 500$, the relationship between the drag coefficient obtained from CFD and the Reynolds number is relatively linear whereas the drag coefficients estimated using the empirical drag models show a more curvilinear behaviour. One possible explanation for this can be the effect of particle morphology. The values of C_D obtained through CFD, accurately reflect the particles' actual morphology since in CFD the pressure and velocity fields of the fluid are calculated on and around the actual surface of the particle. While the empirical drag models incorporate a few of the particles' morphological descriptors in their formulation which is based on the drag coefficient formula of a free-falling sphere to account for the particles' geometry. This can lead to the effects of particles' morphology to be more prominent in calculating the drag coefficient utilising CFD compared to using the empirical drag models. One example for this claim is the drag coefficient C_D versus the Reynolds number *Re* graphs for several values of particle sphericity presented in [46] (and reproduced in Figure S4 in the Supplementary Information document) which clearly show as the values of particle sphericity drop from 1.0, which corresponds to a perfect sphere, the C_D versus *Re* graphs lose their curvature.

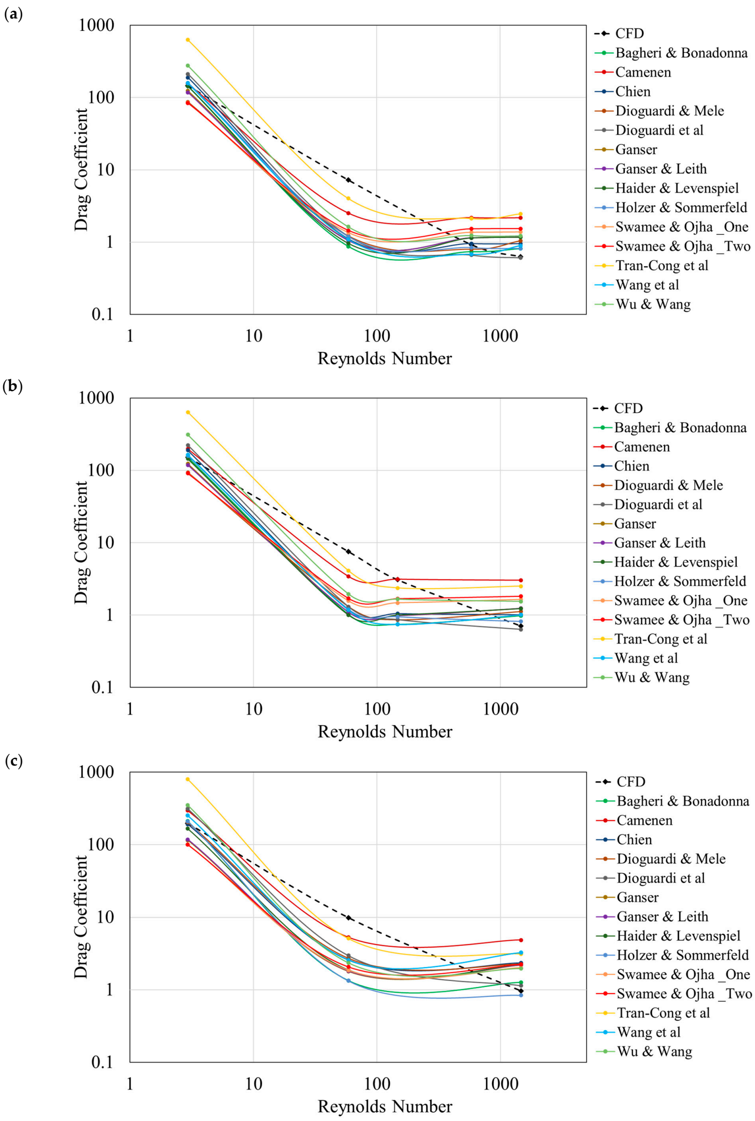

Figure 13. Comparison of the values of the drag coefficient obtained through CFD with the results of the empirical drag models [8–20] versus the Reynolds number for (**a**) compact, (**b**) flat, and (**c**) elongated particle.

3.8. Disscussion on How to Choose the Most Suitable Emrprical Drag Model Based on Particle Morphology and Flow Regime

In this research, the drag coefficient of non-spherical particles with varied morphologies has been investigated at various flow regimes for a range of the Reynolds number. Table 9 condenses all the findings to fulfil the goal of the current research in presenting a clear guideline for choosing the most suitable drag model for numerical modelling by comparing all the 14 empirical drag models, their operational Reynolds number range, their approach in accounting for particle morphology and orientation, and their accuracy for each morphology category which is defined as excellent (Error < 40%), good (40% < error < 80%), moderate (80% < error < 120%), and poor (error > 120%).

Table 9. Comparison of the empirical drag models, their operational Reynolds number range, approach in accounting for particle morphology and orientation, and accuracy for each morphology category defined as E for excellent (error < 40%), G for good (40% < error < 80%), M for moderate (80% < error < 120%), and P for poor (error > 120%).

Drag Model	Reynolds Number Range	Shape Implementation		Drag Model Accuracy												
				Reynolds Number Order of Magnitude												
				O(1)			O(10)			O(100)				O(1000)		
				Particle Shape Category												
		Descriptors	Orientation	Comp.	Flat	Elong.	Comp.	Flat	Elong.	Comp.	Flat	Elong.	Bladed	Comp.	Flat	Elong.
Bagheri and Bonadonna [8]	$[e^{-3}\ 3e^{5}]$	$\overline{e} = I/L$ $\overline{f} = S/I$	No	E	E	E	M	M	M	G	G	G	E	E	E	E
Haider and Levenspiel [9]	$[e^{-1}\ e^{5}]$	True Sphericity [34]	No	E	E	E	M	M	M	G	G	E	E	M	G	P
Ganser [10]	$[e^{-3}\ e^{5}]$	True Sphericity [34]	No	E	E	G	M	M	M	G	G	E	E	M	G	M
Ganser [10] and Leith [11]	$[e^{-3}\ e^{5}]$	True Sphericity [34]	Crosswise Sphericity [12]	E	E	E	M	M	M	G	G	E	E	M	G	M
Hölzer and Sommerfeld [12]	$[e^{-3}\ 3e^{5}]$	True Sphericity [34]	Crosswise and Lengthwise Sphericity [12]	E	E	E	M	M	M	E	G	G	G	E	E	E
Tran-Cong et al. [13]	$[15e^{-2}\ 15e^{2}]$	Surface Circularity [13]	Max or Min Projection Perimeter for Surface Circularity [13]	P	P	P	G	G	G	G	E	E	E	P	P	P
Swamee and Ojha [14]	$[1\ e^{4}]$	Corey Sphericity [41]	No	E	E	G	G	G	G	G	E	E	G	P	P	M
Camenen [15]	$[e^{-1}\ e^{4}]$	Corey Sphericity [41] Roundness [45]	No	G	E	G	G	G	G	G	E	E	P	P	P	P
Wu and Wang [16]	$[e^{-2}\ e^{5}]$	Corey Sphericity [41]	No	M	M	G	G	G	G	G	E	E	E	M	M	M
Wang et al. [17]	$[e^{-2}\ 37e^{2}]$	Shape Factor [42]	No	E	E	E	M	M	G	G	G	E	E	G	G	P
Dioguardi and Mele [18]	$[e^{-3}\ e^{4}]$	Shape Factor [42]	No	E	E	E	M	M	G	G	G	E	E	G	G	P
Dioguardi et al. [19]	$[3e^{-2}\ e^{4}]$	Shape Factor [42]	No	G	G	G	M	M	G	G	G	E	E	E	E	E
Chien [20]	$[e^{-3}\ e^{4}]$	True Sphericity [34]	No	E	E	E	M	M	G	E	G	E	G	G	G	P

Table 9 shows that the performance of the empirical drag models can be investigated through several lenses:

The flow regime (i.e., the order of magnitude of the Reynolds number): The overall accuracy of the empirical drag models is highest when the Reynolds numbers lie within the order of magnitude of O(100). The second and third highest overall accuracy of the empirical drag models correspond to the Reynolds numbers within the order of magnitude of O(1) and O(10), respectively. As the order of the Reynolds number reaches O(1000), most of the empirical drag models start to work somewhat poorly.

The particle morphology implementation (i.e., particle shape descriptors): The empirical drag models that use the particle's true sphericity (a.k.a. Wadell's sphericity) [34] namely Haider and Levenspiel [9], Ganser [10], Ganser and Leith [11], Hölzer and Sommerfeld [12], and Chien [20] as well as the models that use Dellino's shape factor [42] namely Wang et al. [17], Dioguardi and Mele [18], and Dioguardi et al. [19] offer higher accuracies when the Reynolds numbers lie within the orders of magnitude of either O(1) or O(100).

The empirical drag models that use Corey's sphericity [41] namely Swamee and Ojha [14], Camenen [15], and Wu and Wang [16] perform well for the Reynolds numbers within the orders of magnitude of O(1) to O(100).

The only model that uses the surface circularity [13] namely Tran-Cong et al. [13] results in high accuracy for the Reynolds numbers within the orders of magnitude of O(10) to O(100). The model by Bagheri and Bonadonna [8] performs well or all Reynolds numbers the orders of magnitude aside from O(10).

The particle morphology category: For the particles with compact and flat morphologies the most accurate choice of the empirical drag models are the ones that use either the particle's true sphericity (a.k.a. Wadell's sphericity) [34] or Dellino's shape factor [42] to implement the particle morphology. The empirical drag models that use Dellino's shape factor [42] offer better accuracy for elongated particles. For bladed particles almost all drag models other than Camenen [15] model, the only one using roundness [45], perform well. The accuracy of the drag model by Bagheri and Bonadonna [8] is high enough for most particle morphologies.

4. Conclusions

In this research, the drag coefficient of regular and irregular particles operating in the intermediate flow regime was investigated using numerical simulation and empirical models. The CFD results are provided as illustrative benchmarks for comparison with the empirical models. For regular ellipsoidal particles, it was shown that the minimum error percentage with which the drag coefficient can be estimated for the entire range of ellipsoids' aspect ratios is 40% and the model proposed by Ganser is able to provide it. Irregular particles from each of the four morphology categories of Zingg chart, namely, compact, flat, elongated, and bladed were selected and positioned at eight orientations and the drag coefficients were calculated. The drag coefficient was proved to be dependent on the particles' orientation and proportional to the ratio of the drag force to the area facing the flow. The Empirical drag models proposed by Camenen and Tran-Cong et al. showed the most accuracy for the compact particles compared to the value obtained through CFD. For the flat and elongated particles, the model presented by Swamee and Ojha for natural sediments and crushed rock fragments, respectively, proved to be efficient. The models proposed by Ganser and Leith result in the minimum error for bladed particles. Additionally, single-sphere representations of the irregular particles were studied through both numerical simulation and empirical models. A key conclusion is that the single sphere representation can be suitable for estimating the drag force of the compact particles and some flat particles with higher sphericities, whereas it is inaccurate for the elongated and bladed particles resulting in an error near 40%. The inscribed sphere was proven to be the most accurate representation for the estimation of the drag coefficient especially for the compact particles. Investigating the accuracy of the empirical drag models over a range of the Reynolds number showed that the accuracy of majority of the empirical drag models is below 40% difference with the CFD data for the Reynolds number of the order of magnitude of O(1). When the Reynolds number was within the order of magnitude of O(10), the accuracy of the empirical drag models dramatically decreased since all the drag models severely underestimated the value of the drag coefficient with above 45% difference with the CFD data. For the Reynolds numbers with the orders of magnitude of O(100), only a few of the empirical drag models resulted in differences of over 40% compared to CFD. The highest Reynolds number order of magnitude of O(1000) investigated here showed that only four empirical drag models offer accuracy of below 40% difference compared to CFD with the majority of the drag models overestimating the value of the drag coefficient.

Supplementary Materials: The following supporting information can be downloaded at: https://www.mdpi.com/article/10.3390/powders4040029/s1. Figure S1: Flat RCG granule positioned at orientation (a) 1, (b) 2, (c) 3, (d) 4, (e) 5, (f) 6, (g) 7, and (h) 8; Figure S2: Elongated rice grain positioned at orientation (a) 1, (b) 2, (c) 3, (d) 4, (e) 5, (f) 6, (g) 7, and (h) 8; Figure S3: Bladed RCG granule positioned at orientation (a) 1, (b) 2, (c) 3, (d) 4, (e) 5, (f) 6, (g) 7, and (h) 8; Figure S4: Figure S4 Reproduction of the drag coefficient C_D versus the Reynolds number Re graphs for several values of particle sphericity Ψ presented in [46]; Table S1: Drag force, area, and drag coefficient of compact particles positioned at different orientations obtained from the CFD simulations; Table S2: Drag force, area, and drag coefficient of flat, elongated, and bladed particles positioned at different orientations obtained from the CFD simulations; Table S3: Drag coefficient and their error for the compact rounded particle positioned at eight orientations obtained from the CFD Simulations and using empirical drag models; Table S4: Drag coefficient and their error for the compact angular particle positioned at eight orientations obtained from the CFD simulations and using empirical drag models; Table S5: Drag coefficient and their error for the flat RCG particle positioned at eight orientations obtained from the CFD simulations and using empirical drag models; Table S6: Drag coefficient and their error for the elongated rice grain positioned at eight orientations obtained from the CFD Simulations and using empirical drag models; Table S7: Drag coefficient and their error for the bladed RCG particle positioned at eight orientations obtained from the CFD Simulations and using empirical drag models.

Author Contributions: Conceptualization, S.M. and S.N.; methodology, S.M. and S.N.; software, S.M.; validation, S.M.; formal analysis, S.M.; investigation, S.M. and S.N.; resources, S.N.; data curation, S.M.; writing—original draft preparation, S.M.; writing—review and editing, S.M. and S.N.; visualization, S.M.; supervision, S.N.; project administration, S.N.; funding acquisition, S.N. All authors have read and agreed to the published version of the manuscript.

Funding: This research was funded by the UK Engineering and Physical Sciences Research Council (EPSRC) grant No. EP/V053655/1 RAILSANDING—Modelling Particle Behaviour in the Wheel-Rail Interface.

Data Availability Statement: The original contributions presented in this study are included in the article/Supplementary Materials. Further inquiries can be directed to the corresponding author.

Conflicts of Interest: The authors declare no conflicts of interest.

Abbreviations

The following abbreviations were used in this manuscript:

CFD	Computational Fluid Dynamics
Comp.	Compact Particle
DEM	Discrete Element Method

DNS	Direct Numerical Simulation
Elong.	Elongated Particle
LBM	Lattice Boltzmann Method
IBM	Immersed Boundary Method
RCG	Recycled Crushed Glass
μCT	X-ray micro-Computed Tomography
FVM	Finite Volume Method
SIMPLE	Semi-Implicit Method for Pressure-Linked Equations
WALE	Wall Adapting Local Eddy-Viscosity
DoX	Design of eXperiment

References

1. Saad, M.; Sadoudi, A.; Rondet, E.; Cuq, B. Morphological Characterization of Wheat Powders, How to Characterize the Shape of Particles? *J. Food Eng.* **2011**, *102*, 293–301. [CrossRef]
2. Abdel-Hamid, S.; Alshihabi, F.; Betz, G. Investigating the Effect of Particle Size and Shape on High Speed Tableting through Radial Die-Wall Pressure Monitoring. *Int. J. Pharm.* **2011**, *413*, 29–35. [CrossRef]
3. Maramizonouz, S.; Nadimi, S.; Skipper, W.; Lewis, R. CFD-DEM Modelling of Particle Entrainment in Wheel-Rail Interface: A Parametric Study on Particle Characteristics. *Railw. Eng. Sci.* **2025**, *33*, 259–270. [CrossRef]
4. Kozlowska, J.; Prus, W.; Stachowiak, N. Microparticles based on Natural and Synthetic Polymers for Cosmetic Applications. *Int. J. Biol. Macromol.* **2019**, *129*, 952–956. [CrossRef] [PubMed]
5. Tsuchiyama, A.; Sakurama, T.; Nakano, T.; Uesugi, K.; Ohtake, M.; Matsushima, T.; Terakado, K.; Galimov, E.M. Three-Dimensional Shape Distribution of Lunar Regolith Particles Collected by the Apollo and Luna Programs. *Earth Planets Space* **2022**, *74*, 172. [CrossRef]
6. White, F.M. *Fluid Mechanics*; Tata McGraw-Hill Education: Singapore, 1979.
7. Crowe, C.T.; Michaelides, E.E. *Multiphase Flow Handbook*; Taylor & Francis: New York, NY, USA, 2006.
8. Bagheri, G.; Bonadonna, C. On the Drag of Freely Falling Non-Spherical Particles. *Powder Technol.* **2016**, *301*, 526–544. [CrossRef]
9. Haider, A.; Levenspiel, O. Drag Coefficient and Terminal Velocity of Spherical and Nonspherical Particles. *Powder Technol.* **1989**, *58*, 63–70. [CrossRef]
10. Ganser, G.H. A Rational Approach to Drag Prediction of Spherical and Nonspherical Particles. *Powder Technol.* **1993**, *77*, 143–152. [CrossRef]
11. Leith, D. Drag on Nonspherical Objects. *Aerosol Sci. Technol.* **1987**, *6*, 153–161. [CrossRef]
12. Hölzer, A.; Sommerfeld, M. New Simple Correlation Formula for the Drag Coefficient of Non-Spherical Particles. *Powder Technol.* **2008**, *184*, 361–365. [CrossRef]
13. Tran-Cong, S.; Gay, M.; Michaelides, E.E. Drag Coefficients of Irregularly Shaped Particles. *Powder Technol.* **2004**, *139*, 21–32. [CrossRef]
14. Swamee, P.K.; Ojha, C.S.P. Drag Coefficient and Fall Velocity of Nonspherical Particles. *J. Hydraul. Eng.* **1991**, *117*, 660–667. [CrossRef]
15. Camenen, B. Simple and General Formula for the Settling Velocity of Particles. *J. Hydraul. Eng.* **2007**, *133*, 229–233. [CrossRef]
16. Wu, W.; Wang, S.S. Formulas for Sediment Porosity and Settling Velocity. *J. Hydraul. Eng.* **2006**, *132*, 858–862. [CrossRef]
17. Wang, Y.; Zhou, L.; Wu, Y.; Yang, Q. New Simple Correlation Formula for the Drag Coefficient of Calcareous Sand Particles of Highly Irregular Shape. *Powder Technol.* **2018**, *326*, 379–392. [CrossRef]
18. Dioguardi, F.; Mele, D. A New Shape Dependent Drag Correlation Formula for Non-Spherical Rough Particles. Experiments and Results. *Powder Technol.* **2015**, *277*, 222–230. [CrossRef]
19. Dioguardi, F.; Mele, D.; Dellino, P. A New One-Equation Model of Fluid Drag for Irregularly Shaped Particles Valid over a Wide Range of Reynolds Number. *J. Geophys. Res. Solid Earth* **2018**, *123*, 144–156. [CrossRef]
20. Chien, S.-F. Settling Velocity of Irregularly Shaped Particles. *SPE Drill. Complet.* **1994**, *9*, 281–289. [CrossRef]
21. Lu, Y.; Wei, L.; Wei, J. A Numerical Study of Bed Expansion in Supercritical Water Fluidized Bed with a Non-Spherical Particle Drag Model. *Chem. Eng. Res. Des.* **2015**, *104*, 164–173. [CrossRef]
22. Gidaspow, D. *Multiphase Flow and Fluidization: Continuum and Kinetic Theory Descriptions*; Academic Press: Cambridge, MA, USA, 1994.
23. Di Felice, R. The Voidage Function for Fluid-Particle Interaction Systems. *Int. J. Multiph. Flow* **1994**, *20*, 153–159. [CrossRef]
24. Beetstra, R.; van der Hoef, M.A.; Kuipers, J. Drag Force of Intermediate Reynolds Number Flow Past Mono-and Bidisperse Arrays of Spheres. *AIChE J.* **2007**, *53*, 489–501. [CrossRef]
25. Stokes, G.G. On the Effect of the Internal Friction of Fluids on the Motion of Pendulums. In *Mathematical and Physical Papers*; Stokes, G.G., Ed.; Cambridge Library Collection—Mathematics; Cambridge University Press: Cambridge, UK, 2009; Volume 3, pp. 1–10.

26. Morsi, S.; Alexander, A. An Investigation of Particle Trajectories in Two-Phase Flow Systems. *J. Fluid Mech.* **1972**, *55*, 193–208. [CrossRef]
27. Syamlal, M.; O'brien, T. Simulation of Granular Layer Inversion in Liquid Fluidized Beds. *Int. J. Multiph. Flow* **1988**, *14*, 473–481. [CrossRef]
28. Koch, D.L.; Hill, R.J. Inertial Effects in Suspension and Porous-Media Flows. *Annu. Rev. Fluid Mech.* **2001**, *33*, 619–647. [CrossRef]
29. Schiller, L.N. A Drag Coefficient Correlation. *Zeit. Ver. Deutsch. Ing.* **1933**, *77*, 318–320.
30. Yang, N.; Wang, W.; Ge, W.; Li, J. CFD Simulation of Concurrent-up Gas–Solid Flow in Circulating Fluidized Beds with Structure-Dependent Drag Coefficient. *Chem. Eng. J.* **2003**, *96*, 71–80. [CrossRef]
31. Rong, L.W.; Dong, K.J.; Yu, A. Lattice-Boltzmann Simulation of Fluid Flow through Packed Beds of Uniform Spheres: Effect of Porosity. *Chem. Eng. Sci.* **2013**, *99*, 44–58. [CrossRef]
32. DallaValle, J.M. *Micromeritics: The Technology of Fine Particles*; Pitman Publishing Cprporation: New York, NY, USA, 1948.
33. Tenneti, S.; Garg, R.; Subramaniam, S. Drag Law for Monodisperse Gas–Solid Systems Using Particle-Resolved Direct Numerical Simulation of Flow Past Fixed Assemblies of Spheres. *Int. J. Multiph. Flow* **2011**, *37*, 1072–1092. [CrossRef]
34. Wadell, H. Volume, Shape, and Roundness of Rock Particles. *J. Geol.* **1932**, *40*, 443–451. [CrossRef]
35. Maramizonouz, S.; Nadimi, S.; Skipper, W.; Lewis, R. Characterisation and Tribological Testing of Recycled Crushed Glass as an Alternative Rail Sand. *Proc. Inst. Mech. Eng. Part F J. Rail Rapid Transit* **2023**, *237*, 1353–1358. [CrossRef]
36. Zingg, T. *Beitrag zur Schotteranalyse*; ETH Zurich: Zurich, Switzerland, 1935.
37. Angelidakis, V.; Nadimi, S.; Utili, S. Elongation, Flatness and Compactness Indices to Characterise Particle Form. *Powder Technol.* **2022**, *396*, 689–695. [CrossRef]
38. Tagliavini, G.; McCorquodale, M.; Westbrook, C.; Corso, P.; Krol, Q.; Holzner, M. Drag Coefficient Prediction of Complex-Shaped Snow Particles Falling in Air beyond the Stokes Regime. *Int. J. Multiph. Flow* **2021**, *140*, 103652. [CrossRef]
39. Maramizonouz, S.; Nadimi, S. Drag Force Acting on Ellipsoidal Particles with Different Shape Characteristics. *Powder Technol.* **2022**, *412*, 117964. [CrossRef]
40. Nicoud, F.; Ducros, F. Subgrid-Scale Stress Modelling Based on the Square of the Velocity Gradient Tensor. *Flow Turbul. Combust.* **1999**, *62*, 183–200. [CrossRef]
41. Corey, A.T. *Influence of Shape on the Fall Velocity of Sand Grains*; Colorado A & M College: Fort Collins, CO, USA, 1949.
42. Dellino, P.; Mele, D.; Bonasia, R.; Braia, G.; La Volpe, L.; Sulpizio, R. The Analysis of the Influence of Pumice Shape on Its Terminal Velocity. *Geophys. Res. Lett.* **2005**, *32*. [CrossRef]
43. Dellino, P.; La Volpe, L. Image Processing Analysis in Reconstructing Fragmentation and Transportation Mechanisms of Pyroclastic Deposits. The case of Monte Pilato-Rocche Rosse Eruptions, Lipari (Aeolian Islands, Italy). *J. Volcanol. Geotherm. Res.* **1996**, *71*, 13–29. [CrossRef]
44. Krumbein, W.C. Measurement and Geological Significance of Shape and Roundness of Sedimentary Particles. *J. Sediment. Res.* **1941**, *11*, 64–72. [CrossRef]
45. Wentworth, C.K. A Laboratory and Field Study of Cobble Abrasion. *J. Geol.* **1919**, *27*, 507–521. [CrossRef]
46. Rhodes, M. Single Particles in a Fluid. In *Introduction to Particle Technology*; John Wiley & Sons: Hoboken, NJ, USA, 2008; pp. 29–49.